

Research Article

Laser Welding of Dissimilar Metal Joint of 6061 Al Alloy and Al Matrix Composite

Jun Dai ^{1,2}, Banglong Yu,¹ Wei Jiang,¹ Hla Min Htun,³ and Zheng Liu ⁴

¹School of Automotive Engineering, Changshu Institute of Technology, Changshu 215500, China

²Shanghai Key Laboratory of Materials Laser Processing and Modification, Shanghai Jiao Tong University, Shanghai 200240, China

³Department of Mechanical Engineering, Mandalay Technological University, Mandalay 05072, Myanmar

⁴School of Modern Technology, Suzhou Top Institute of Information Technology, Kunshan 215311, China

Correspondence should be addressed to Zheng Liu; 155365966@qq.com

Received 22 October 2018; Revised 2 January 2019; Accepted 23 January 2019; Published 2 May 2019

Academic Editor: Candido Fabrizio Pirri

Copyright © 2019 Jun Dai et al. This is an open access article distributed under the Creative Commons Attribution License, which permits unrestricted use, distribution, and reproduction in any medium, provided the original work is properly cited.

In this paper, dissimilar metal joints of 6061 aluminum alloy and aluminum matrix composite material are investigated by laser welding. TiB₂ particles were added into the lap joint. The welding process, microstructure, and the corrosion properties of welding joints are examined. The results demonstrate that the selected optimization process parameters are laser power 6 kW, welding speed 0.6 mm/s, pulse width 11.5 ms, and laser frequency 4.5 Hz. There are a few obvious pores in the molten pool. Al₂Ti, Fe₂Si, and Al_{0.5}Fe₃Si_{0.5} are present in the microstructure. During the welding process, some TiB₂ particles are decomposed and reacted with molten Al. Other TiB₂ particles are nucleated and solidified, and the excess TiB₂ particles are pushed to the grain boundaries by molten Al. TiB₂ particles are wetted well by molten matrix metal. The corrosion resistance of alloys in different conditions decreased in the following order: the weld beam >6061 Al > AMC.

1. Introduction

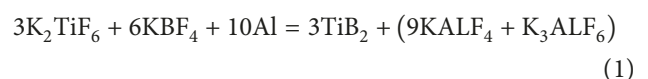
Aluminum alloys and aluminum matrix composites (AMCs) are two highly important lightweight metals currently used in many fields such as automotive, electronics, and aerospace industries because of their good formability and lightweight. So the issues of joining Al alloy and AMC cannot be avoided. Up to now, there are numerous reinforcing phases for AMC, most commonly TiC, ZrB₂, nanotube, and so on [1, 2]. At present, there are many researches on the welding of AMC enhanced by SiC, Al₂O₃, and B₄C [3–8], but there are few reports on pulsed laser welding of TiB₂-reinforced AMC [9–11]. According to the research of constantly high-power laser welding of TiB₂-reinforced AMC [10], it is found that TiB₂ particles have a great influence on the flowability of molten pool and there is a certain trend in the interface reaction between TiB₂ particles and matrix metal.

Up to now, there are some friction welding processes of dissimilar Al/AMC alloys [12, 13]. But research on Al/AMC laser-welded joints and the corrosion properties of welding

joints is little. This study is intended to investigate Nd-YAG laser welding of dissimilar Al/AMC joints with TiB₂ particles. Welding process is discussed using the orthogonal test. The microstructure and the corrosion properties of laser-welded Al/AMC joints were also discussed.

2. Experimental

AMCs were prepared by using the in situ autogenous method. In the reaction, K₂TiF₆ and KBF₄ salts were added in proper Ti:B ratios to the molten ZL101 aluminum alloy liquid at 850°C, stirred for 30 min at regular intervals (LHS-RLL), and cast in a constrained rod casting (CRC) mold (KTZL-1) at 750°C. The formula of exothermic reaction between mixed salt and metal is as follows:



The size of the test specimens of 6061 Al and AMC material is 100 mm × 50 mm × 1 mm with 99.9% purity TiB₂

particles. The chemical compositions of 6061 Al and AMC are given in Table 1.

The Nd-YAG-pulsed laser source (WF-300) was utilized. Before welding, the oxide film on the surface of the specimen was removed and then cleaned using acetone. After welding, the metallurgical sample was prepared and etched with HF ($\text{HF}:\text{H}_2\text{SO}_4:\text{H}_2\text{O} = 5\%:10\%:85\%$) solution. The microstructures were observed by using the Olympus GX51 optical microscope (OM) and scanning electron microscopy (SEM) Zeiss EVO 18. The chemical compositions were analyzed and identified by using energy-dispersive spectrometry (EDS) and X-ray diffraction (XRD) Bruker APEX II DUO.

The longitudinal section of welding joints is used for the corrosion test. 5% NaCl solution is accompanied by a CS350H electrochemical system. The specimens were treated with metallographic polishing, followed by washing with distilled water and alcohol, and finally dried in warm air before experiment. Open circuit potential measurement immediately began after the specimens were immersed into the solution. For polarization curves, after the immersion of the electrode into the corrosive solution, the working electrode was abandoned at open circuit potential for more than 10 min in order to stabilize the corrosion potential. The polarization started from a cathodic potential of -250 mV relative to the open circuit potential and stopped at an anodic potential where the anodic current increased significantly. The scanning rate was 1 mV/s . 6061 Al, and AMC base metal are also tested as contrast.

3. Results and Discussion

3.1. Welding Process. The samples were lap welded using the Nd-YAG laser welding technique. A schematic diagram of the process is shown in Figure 1. Welding process is discussed using the orthogonal test. In this experiment, the parameters of power (P), laser frequency (f), and velocity (V) were selected. The parameters are given in Table 2.

Nine welding joints can be deserved utilizing the parameters. Welding penetration and welding width of every welding joint are tested using OM. The results are presented in Table 3. Scores of every welding joint were calculated in accordance with four aspects of weld penetration, weld width, weld evenness and uniformity, and weld defects. The score of each aspect was 10 points, with a total of 40 points. K_1 , K_2 , and K_3 are the total scores of each parameter. k_1 , k_2 , and k_3 are the average values of each parameter. The consequences of the orthogonal test are displayed in Table 4.

Through the results and range analysis, the laser power difference reaches 1.67; the laser frequency range is 1.51, and the velocity range is 1.33. The laser power is the most significant influence on weld formation, followed by laser frequency and welding speed. According to the previous experimental results, the selected optimization process parameters are laser power is 6 kW, laser frequency is 4.5 Hz, welding speed is 0.6 mm/s, the protection of argon gas flow 15 L/min, laser defocus is 0, and the laser pulse width is 11.5 ms.

3.2. Microstructure. The microstructure of welding joints is illustrated in Figure 2. It can be seen from Figure 2(a) that the

TABLE 1: The chemical composition of two alloys (wt.%).

Alloy	Al	Zn	Mn	Si	Fe	Cu	TiB ₂	Ti	Mg
AMC	Bal.	0.01	0.04	4	0.05	0.05	5		7
6061 Al	Bal.	0.25	0.15	0.4	0.7	0.16		0.1	1

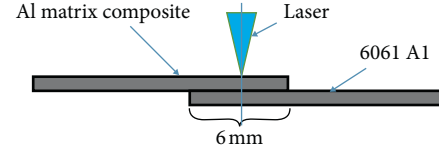


FIGURE 1: Schematic diagram of the laser welding process.

TABLE 2: Parameters of the orthogonal test.

Level	Power (kW)	Laser frequency (Hz)	Velocity (mm/s)
1	5	4	0.6
2	5.5	4.5	0.8
3	6	5	1

TABLE 3: The results of welding penetration and width (μm).

Number	Width	Penetration
1	968.19	437.92
2	938.56	488.14
3	1010.40	506.24
4	1058.81	490.47
5	1149.63	547.38
6	1158.64	567.10
7	1200.25	683.38
8	1331.10	828.14
9	1357.30	834.95

TABLE 4: The results of the orthogonal test.

Number	P (kW)	f (Hz)	V (mm/s)	Score
1	5	4	0.6	26
2	5	4.5	0.8	27
3	5	5	1	26
4	5.5	4	0.8	28
5	5.5	4.5	1	28
6	5.5	5	0.6	27
7	6	4	1	28
8	6	4.5	0.6	27
9	6	5	0.8	29
K_1	79	79	80	
K_2	83	82	84	
K_3	84	85	82	
k_1	26.33	26.33	26.67	
k_2	26.67	27.33	28	
k_3	28	29.52	27.33	
Range	1.67	1.51	1.33	

dissimilar metal joint is good. There is no obvious defect in the joint. The microstructure of the fusion zone is shown in Figure 2(b). Many equiaxed grains are there in the fusion zone.

The map of element is presented in Figure 3. It can be seen that Al element is the main element in the welding joint.

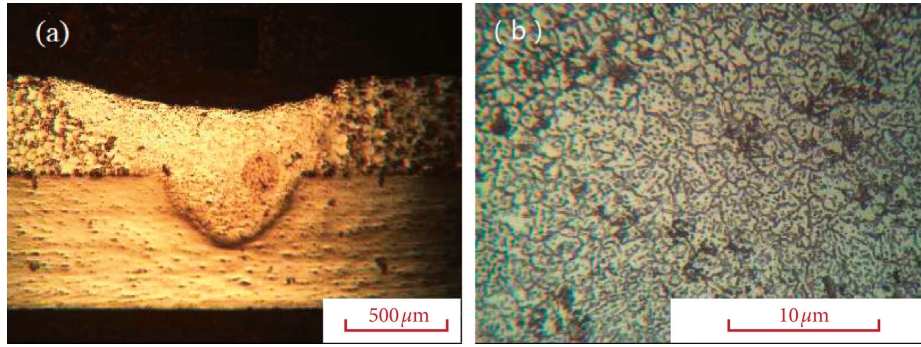
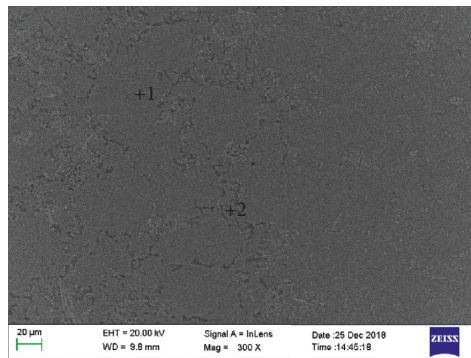
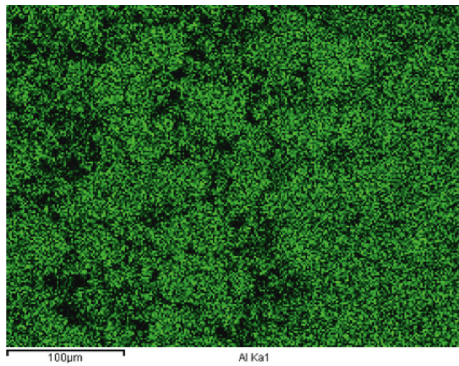


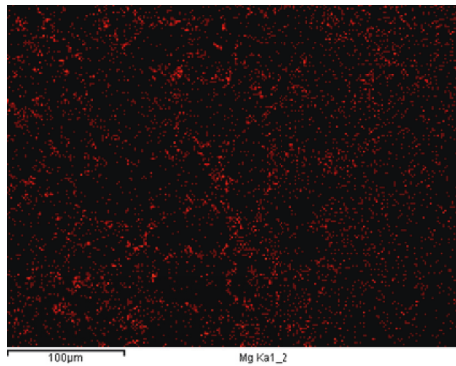
FIGURE 2: Microstructure of welding joint. (a) Cross section. (b) Microstructure of the fusion zone.



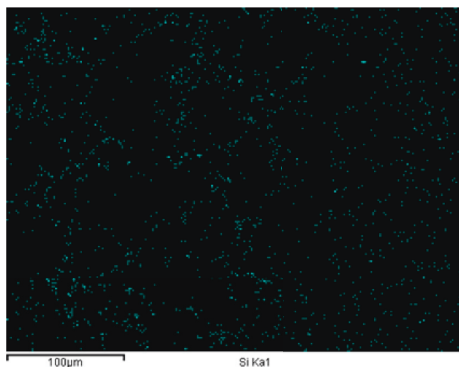
(a)



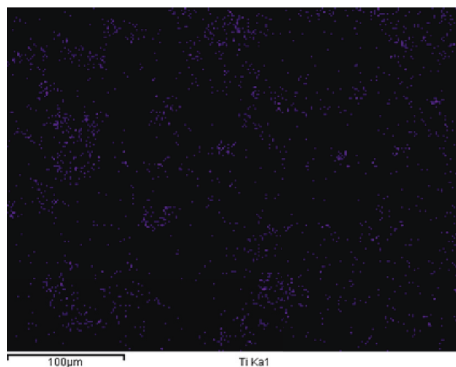
(b)



(c)



(d)



(e)

FIGURE 3: Map of the element.

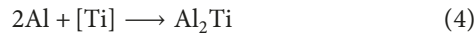
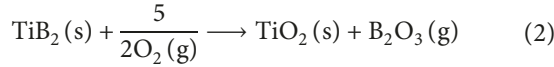
Ti and Si elements are mostly distributed along the grain boundary. The consequences of EDS of different locations (Figure 3) are shown in Table 5. The content of Ti element in

the grain boundary is about 2 times of that in the crystal. Si is mainly distributed at the grain boundary and contains about three times as much as in the crystal.

TABLE 5: EDS results at different locations (at.%).

Location	Al	Mg	Ti	Si
1	95.18	2.76	1.54	0.52
2	90.96	3.67	3.73	1.64

It can be observed in the reaction formula (2) that some TiB_2 particles are irradiated by laser radiation and oxidation, Ti and B atoms react with O, and Ti-B covalent bond breaks and released. There are accompanied by a reaction with liquid Al to generate AlB_{12} and Al_2Ti with higher temperature, as shown in reactions (3) and (4):



In order to assess the stability of the precipitated phases, it is crucial to have a reliable calculation for the Gibbs free energy ΔG of the reaction formulas (2) to (4). In these reactions, ΔG is not only a function of temperature but also dependent on the concentration of reactants and products. Thus, the Gibbs free energy ΔG of the reaction formulas (2) to (4) can be expressed as follows:

$$\begin{aligned} \Delta G_{\text{TiO}_2} + \Delta G_{\text{TiO}_2} &= \Delta G_{\text{TiO}_2}^\theta + \Delta G_{\text{B}_2\text{O}_3}^\theta - RT \ln \alpha \\ &\quad - 2RT \ln \alpha_{\text{B}} - 5RT \ln \alpha_{\text{O}} \\ \Delta G_{\text{AlB}_{12}} &= \Delta G_{\text{AlB}_{12}}^\theta - RT \ln \alpha_{\text{Al}} - 12RT \ln \alpha_{\text{B}} \\ \Delta G_{\text{Al}_2\text{Ti}} &= \Delta G_{\text{Al}_2\text{Ti}}^\theta - 2RT \ln \alpha_{\text{Al}} - RT \ln \alpha_{\text{Ti}} \end{aligned} \quad (5)$$

where ΔG^θ is the standard Gibbs free energy, and the standard Gibbs free energy ΔG^θ for the different substances is listed in Table 6, where α_i represents the activity of the element i in the melting composite. The activity of TiO_2 , B_2O_3 , AlB_{12} , and Al_2Ti in molten Al is approximately 1, so the Gibbs free energy ΔG of the reaction formulas (2) to (4) is approximately equal to the standard Gibbs formation free energy of unlike substances.

It can be indicated in Table 6 that the Gibbs free energies of all products are less than zero [14], so these reactions are likely to occur during laser welding of TiB_2 enhanced AMC. The consequences can theoretically explain that TiB_2 particles react with O_2 present in the air or dissolve in the molten pool to produce TiO_2 and B_2O_3 . The results can also illustrate that TiB_2 will react with the Al matrix to produce AlB_{12} and Al_2Ti when it is resurrounded by molten Al. Since the maximum temperature of the molten pool is lower than the boiling point of Al (2740 K), that is, less than 3000 K, negative Gibbs free energy promotes the reaction of molten TiB_2 with Al and O atoms.

The results of XRD of the weld beam are presented in Figure 4. It can be assumed that mainly Al, Al_2Ti , Fe_2Si , and $\text{Al}_{0.5}\text{Fe}_3\text{Si}_{0.5}$ are present. During the welding process, some TiB_2 particles are decomposed and reacted with molten Al. Some complex products are generated during the welding

TABLE 6: ΔG values of formation to TiO_2 , Al_2Ti , B_2O_3 , and AlB_{12} .

Reaction	ΔG^θ expression/ ($\text{J}\cdot\text{mol}^{-1}$)
$\text{TiB}_2(\text{s}) + 5/2\text{O}_2(\text{g}) \longrightarrow \text{TiO}_2(\text{s}) + \text{B}_2\text{O}_3(\text{g})$	$-1470544.4 + 124.2 \text{ T}$
$\text{Al} + 12[\text{B}] \longrightarrow \text{AlB}_{12}$	$-220000 + 7.5 \text{ T}$
$2\text{Al} + [\text{Ti}] \longrightarrow \text{Al}_2\text{Ti}$	$-144242 + 21 \text{ T}$

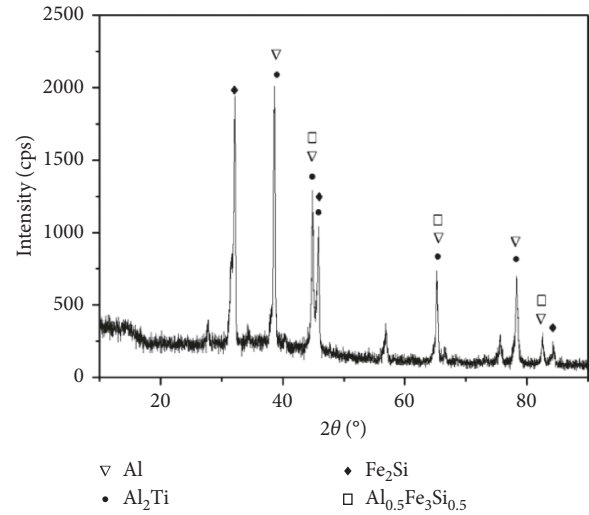


FIGURE 4: XRD results of the weld beam.

process. Other TiB_2 particles are nucleated and solidified, and the excess TiB_2 are pushed to the grain boundaries by molten Al.

In the process of welding solidification, the interfacial interaction model is proposed by combining the mutual wettability between the solid phase and liquid phase/particle three phases, as shown in Figure 5. Assuming that the contact angle θ between the particles and the liquid/solid interface during the solidification process is determined by the interfacial energy between the three phases [15], and there are two states: (1) $\theta < 90^\circ$, as shown in Figure 5(a), the particles are captured because $r_{\text{PL}} > r_{\text{SP}}$, and wetting between particles and solid phase is more likely to occur and (2) $\theta > 90^\circ$, as shown in Figure 5(b), where the particles are repelled by the liquid/solid interface.

For high-interface energy systems such as AMC, the most important thing in the welding process is to change the interface energy in order to encourage the combination of particles and solid phase and form a uniform distribution. In this paper, the interfacial energy of each phase in AMC is modified by TiB_2 particles and introducing the pulsed laser during the welding process. The interaction between the particles and the liquid/solid interface is controlled to a certain extent. Some particles are well wetted by molten matrix metal, and the distribution of the particles is improved in the matrix metal.

3.3. Corrosion Properties. The potentiodynamic polarization curves for different samples in 5% NaCl solution are presented in Figure 6. The curves of the cathodic region to some extent

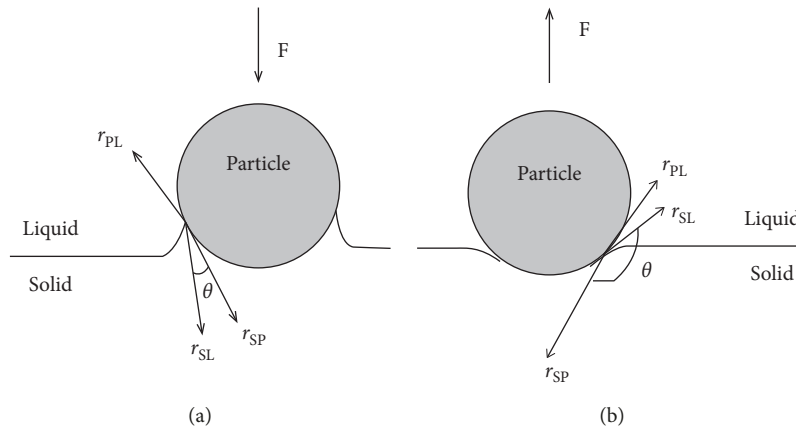


FIGURE 5: Reaction model of interface between solid phase and liquid phase. (a) $\theta < 90^\circ$ (b) $\theta > 90^\circ$.

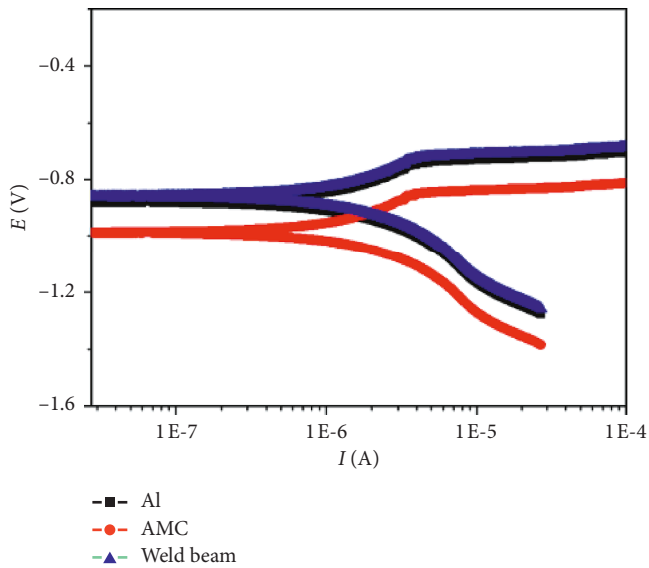


FIGURE 6: The potentiodynamic polarization curves for different samples in 5% NaCl solution.

represent the polarization behaviour of the noncorroded surface of the specimen and the reaction of hydrogen evolution. As the potential increases gradually to a relatively high (anodic) potential, corrosion starts on the surface and becomes more severe with the potential increase. The corrosion resistance of alloys in different conditions decreased in the following order: the weld beam > 6061 Al > AMC.

The TiB_2 phase is dispersed in the weld beam, which will obviously reduce the corrosion rate of the weld beam. The schematic diagram of TiB_2 phase retarding corrosion is displayed in Figure 7. Therefore, the corrosion resistance of the weld is the best. The content of TiB_2 in AMC is 5%, which is not enough to improve the corrosion rate of aluminum alloy. Therefore, the corrosion rate of AMC is the fastest.

4. Conclusions

- (1) According to the results of the orthogonal test, the laser power is the most important influence on weld

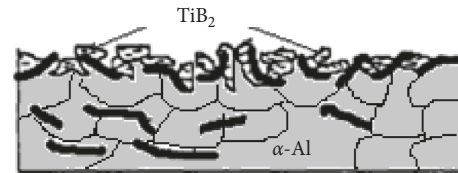


FIGURE 7: Schematic diagram of TiB_2 phase retarding corrosion.

formation of dissimilar 6061 Al/AMC joints with TiB_2 , followed by laser frequency and welding speed. The selected optimization process parameters of 1 mm 6061 Al/AMC lap welding are laser power is 6 kW, laser frequency is 4.5 Hz, the velocity is 0.6 mm/s, laser pulse width is 11.5 ms, the protection of argon gas flow is 15 L/min, and laser defocus is 0.

- (2) Mostly Al, Al_2Ti , Fe_2Si , and $\text{Al}_{0.5}\text{Fe}_3\text{Si}_{0.5}$ are present in the microstructure. During the welding process, some TiB_2 particles are decomposed and reacted with molten Al. Other TiB_2 particles are nucleated and solidified, and the excess TiB_2 particles are pushed to the grain boundaries by molten Al. TiB_2 particles are wetted well by molten Al.
- (3) The corrosion resistance of alloys in different conditions decreased in the following order: the weld beam > 6061 Al > AMC.

Data Availability

The data used to support the findings of this study are included within the article.

Conflicts of Interest

The authors declare that they have no conflicts of interest.

Acknowledgments

This research was financially supported by the National Natural Science Foundation of China (Grant no. 51505040), Qing Lan Project of Jiangsu Province, and Jiangsu Key

Laboratory of Large Engineering Equipment Detection and Control under Grant no. JSKLEDC201507. The project was supported by Open Fund of Shanghai Key Laboratory of Materials Laser Processing and Modification (Grant no. MLPM2017-1). This project was also supported by Post-doctoral Research Funding Plan in Jiangsu Province (Grant no. 2018K055C).

References

- [1] Q. Liu, L. Ke, F. Liu, C. Huang, and L. Xing, "Microstructure and mechanical property of multi-walled carbon nanotubes reinforced aluminum matrix composites fabricated by friction stir processing," *Materials & Design*, vol. 45, pp. 343–348, 2013.
- [2] D. Jeyasimman, S. Sivasankaran, K. Sivaprasad, R. Narayanasamy, and R. S. Kambali, "An investigation of the synthesis, consolidation and mechanical behaviour of Al 6061 nanocomposites reinforced by TiC via mechanical alloying," *Materials & Design*, vol. 57, pp. 394–404, 2014.
- [3] T. M. Yue, J. H. Xu, and H. C. Man, "Pulsed Nd-YAG laser welding of A SiC particulate reinforced aluminium alloy composite," *Applied Composite Materials*, vol. 4, no. 1, pp. 53–64, 1997.
- [4] J. Guo, P. Gougeon, and X.-G. Chen, "Study on laser welding of AA1100-16vol.% B4C metal-matrix composites," *Composites Part B: Engineering*, vol. 43, no. 5, pp. 2400–2408, 2012.
- [5] L. M. Liu, M. L. Zhu, and J. T. Niu, "Study on behavior of reinforcement in molten pool for submicron composite Al₂O₃/6061Al during laser welding," *China Welding*, vol. 10, pp. 99–103, 2001.
- [6] J. Zhang, X. S. Feng, and H. Huang, "Micro friction stir welded lap joint of thin Al-alloy/SiC reinforced Al composite, rare metal," *Metallurgical and Materials Engineering*, vol. 45, pp. 720–726, 2016.
- [7] K. Deepandurai and R. Parameshwaran, "Multiresponse optimization of FSW parameters for cast AA7075/SiCp composite," *Materials and Manufacturing Processes*, vol. 31, no. 10, pp. 1333–1341, 2016.
- [8] J. T. Niu, L. M. Liu, and Y. H. Tian, "Pulsed laser welding of SiCw/6061Al matrix compositions," *Applied Lasers*, vol. 19, pp. 1–3, 1999.
- [9] H. C. Cui, F. G. Lu, X. H. Tang, and S. Yao, "Laser welding of in-situ particulate reinforced aluminum matrix composites," *Transactions of the China Welding Institution*, vol. 31, pp. 68–72, 2010.
- [10] C. Meng, H. C. Cui, F. G. Lu, and X. H. Tang, "Evolution behavior of TiB₂ particles during laser welding on aluminum metal matrix composites reinforced with particles," *Transactions of Nonferrous Metals Society of China*, vol. 23, pp. 1–6, 2013.
- [11] J. Dai, Z. Liu, L. Yang, Y. Wang, C. Y. Zhou, and Y. C. Zhang, "Research on pulsed laser welding of TiB₂-enhanced aluminum matrix composites," *International Journal of Advanced Manufacturing Technology*, vol. 85, no. 1–4, pp. 157–162, 2016.
- [12] O. T. Midling and Ø. Grong, "A process model for friction welding of Al-Mg-Si alloys and Al-SiC metal matrix composites-I. Haz temperature and strain rate distribution," *Acta Metallurgica et Materialia*, vol. 42, no. 5, pp. 1595–1609, 1994.
- [13] K. Kato and H. Tokisue, "Weld interface of friction welded aluminium alloy composite to aluminium alloy joints," *Welding International*, vol. 9, no. 5, pp. 352–356, 1995.
- [14] Y. Liang, J. e. Zhou, S. Dong, and T. Yang, "Thermodynamic analysis of the formation of In-situ reinforced phases in cast Al-4.5Cu alloy," *Journal of Wuhan University of Technology*, vol. 23, no. 3, pp. 342–345, 2008.
- [15] S. S. Wu, "Research advances on behavior of particles in front of solidification interface of MMCs," *Materials Review*, vol. 12, pp. 1–5, 1998.



Hindawi
Submit your manuscripts at
www.hindawi.com

